

## Tunable Terahertz Hybrid Metal–Graphene Plasmons

Mohammad M. Jadidi,<sup>\*,†</sup> Andrei B. Sushkov,<sup>‡</sup> Rachael L. Myers-Ward,<sup>§</sup> Anthony K. Boyd,<sup>§</sup> Kevin M. Daniels,<sup>§</sup> D. Kurt Gaskill,<sup>\*,§</sup> Michael S. Fuhrer,<sup>\*,‡,||</sup> H. Dennis Drew,<sup>\*,‡</sup> and Thomas E. Murphy<sup>\*,†</sup>

<sup>†</sup>Institute for Research in Electronics & Applied Physics, University of Maryland, College Park, Maryland 20742, United States

<sup>‡</sup>Center for Nanophysics and Advanced Materials, University of Maryland, College Park, Maryland 20742, United States

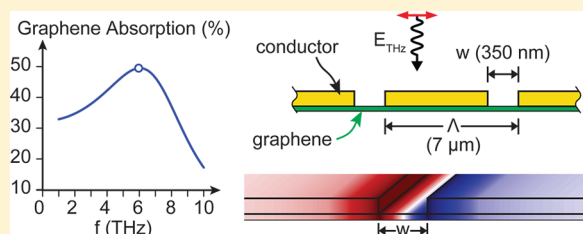
<sup>§</sup>U. S. Naval Research Laboratory, Washington, DC 20375, United States

<sup>||</sup>School of Physics, Monash University, Frankston 3800, Victoria Australia

**S** Supporting Information

**ABSTRACT:** We report here a new type of plasmon resonance that occurs when graphene is connected to a metal. These new plasmon modes offer the potential to incorporate a tunable plasmonic channel into a device with electrical contacts, a critical step toward practical graphene terahertz optoelectronics. Through theory and experiments, we demonstrate, for example, anomalously high resonant absorption or transmission when subwavelength graphene-filled apertures are introduced into an otherwise conductive layer. These tunable plasmon resonances are essential yet missing ingredients needed for terahertz filters, oscillators, detectors, and modulators.

**KEYWORDS:** graphene, terahertz, far-infrared, plasmons, antennas, metamaterials



Among its many outstanding properties, graphene supports terahertz two-dimensional plasma waves: subwavelength charge density oscillations connected with electromagnetic fields that are tightly localized near the graphene sheet.<sup>1,2</sup> When these waves are confined to finite-sized graphene, plasmon resonances emerge that are characterized by alternating charge accumulation at the opposing edges of the graphene. The resonant frequency of such a structure depends on both the size and the surface charge density and can be electrostatically tuned throughout the terahertz range by applying a gate voltage.<sup>3–5</sup> Graphene plasmons have been explored or proposed for use in biosensors,<sup>6</sup> terahertz detectors,<sup>7</sup> terahertz emitters,<sup>8</sup> and a growing number of devices in the nascent field of terahertz optoelectronics. It is increasingly recognized that graphene holds potential for filling a critical gap in terahertz technology.<sup>9–15</sup> The promise of tunable graphene THz plasmonics has yet to be fulfilled, however, because most proposed optoelectronic devices require near total modulation of the absorption or transmission and need antenna coupling<sup>10,15</sup> or electrical contacts to the graphene—constraints that are difficult to meet using existing plasmonic structures. Until now, there was no experimental evidence that two-dimensional plasmons could be confined with conductive boundaries.

In this Letter, we demonstrate a new class of plasmon resonances that occurs when graphene fills a metallic aperture, and we use analytic calculations, numerical simulations, and THz reflection and transmission measurements to confirm the principle of operation. These plasmon modes exploit the unique gate-tunable inductance of graphene to produce a

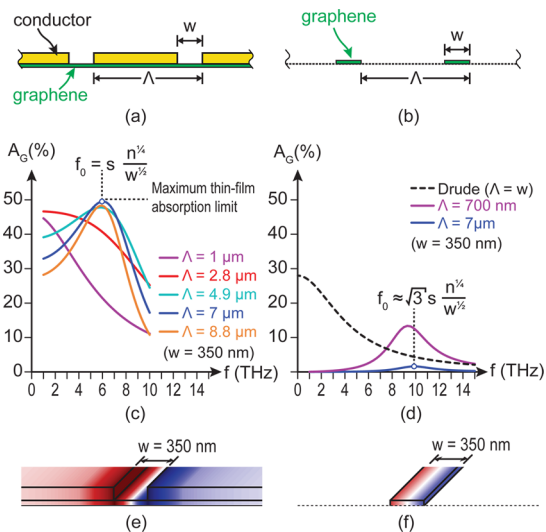
resonance in a metallic structure that, by itself, exhibits no resonance. Unlike graphene ribbons, which absorb only a few percent of incident radiation at the resonant frequency,<sup>4</sup> the new plasmon modes couple strongly to incident terahertz radiation and can achieve maximal absorption in monolayer graphene apertures at a resonance frequency that is gate-tunable. We also introduce an equivalent circuit model that predicts the resonant frequency, line width, and impedance matching condition of the fundamental plasmon mode and can be used for designing graphene plasmonic metamaterials and antenna coupled devices. Additionally, high mobility graphene is predicted to produce a tunable resonance peak in transmission that approaches 100%, which is ideal for THz modulators and tunable bandpass filters.

Figure 1a shows the structure of the metal-contacted graphene plasmonic device considered here, which is comprised of a periodic array of narrow slots in a metallic layer that is patterned on top of a continuous graphene layer. For comparison, in Figure 1b, we also consider an array of isolated graphene ribbons of comparable dimension. In both cases, the period  $\Lambda$  is taken to be small compared to the free-space wavelength. To calculate the plasmon resonances and absorption in these structures, we adapt the method of ref 16 to obtain an integral equation for the in-plane electric field when the structure is illuminated by a normally incident plane

**Received:** August 11, 2015

**Revised:** September 22, 2015

**Published:** September 23, 2015



**Figure 1.** (a) Geometry of hybrid metal–graphene structure considered here. (b) Comparable array of isolated graphene ribbons. (c) Calculated graphene absorption spectrum  $A_G(\omega)$  for the hybrid metal–graphene device with periods of  $\Lambda = 1, 2.8, 4.9, 7,$  and  $8.8 \mu\text{m}$ , for a graphene channel with  $w = 350 \text{ nm}$ ,  $n = 1.5 \times 10^{13} \text{ cm}^{-2}$ , and  $\mu = 1000 \text{ cm}^2 \text{ V}^{-1} \text{ s}^{-1}$ . The upper and lower dielectric regions were assumed to be identical, with  $\epsilon_1 = \epsilon_2 = 5$ , in which case the theoretical maximum thin-film absorption is 50%,<sup>18</sup> indicated by the horizontal dashed line. (d) Calculated absorption spectrum for isolated graphene ribbons with material properties identical to the channels considered in (c), and periods of  $\Lambda = 0.7$  and  $7 \mu\text{m}$ . For comparison, the dashed line indicates the Drude absorption spectrum for a continuous graphene sheet. (e) and (f) Calculated charge density profile at the plasmon resonant frequency for the hybrid metal–graphene device and graphene ribbon, respectively.

wave at frequency  $\omega$  that is linearly polarized in the direction perpendicular to the graphene channels. Details of this theory are provided in the Supporting Information (S1). The resonant modes and fractional absorption in the graphene  $A(\omega)$  is then found by integrating the Joule power density over the graphene ribbon, and normalizing to the incident power of the plane wave. The calculated absorption spectrum reveals all of the dipole-active plasmon resonances and the relative coupling of these modes to radiation. In this Letter, we focus on the fundamental low frequency plasmon mode. Higher order modes resonate at higher frequencies and can also be optimally coupled to the THz radiation.

In Figure 1c we present the theoretically computed absorption spectrum  $A(\omega)$  for several different metal periods  $\Lambda$ , with the graphene ribbon width  $w = 350 \text{ nm}$  held constant. The mobility and carrier density (electron or hole) were taken to be  $\mu = 1000 \text{ cm}^2 \text{ V}^{-1} \text{ s}^{-1}$  and  $n = 1.5 \times 10^{13} \text{ cm}^{-2}$ , respectively. The array shows no discernible plasmon resonance when the period  $\Lambda$  and graphene width  $w$  are comparable, giving instead a Drude-like response. However, when the metal contacts are made much wider than the graphene channel, a strong resonance emerges, characterized by high absorption in the graphene ribbon, at a resonant frequency that scales with  $n^{1/4} w^{-1/2}$ , similar to the plasmon resonances in uncontacted graphene ribbons.<sup>4,17</sup> The surrounding material is assumed to be a uniform dielectric, in which case, the maximum achievable absorption in a two-dimensional layer is 50%<sup>18</sup> (also (S26) in Supporting Information). As shown in Figure 1c, at the resonant frequency, the graphene absorption reaches a peak of

the maximum possible value (50%), even when the geometrical fill factor is only  $w/\Lambda = 1/20$  (5%). This suggests, at plasmon frequency, an extremely high confinement of the THz field in the narrow slots where graphene is located. This makes the metal-graphene scheme an attractive candidate for nonlinear THz plasmonic applications. We note that by using known techniques such as an antireflection coating or a Salisbury screen<sup>19</sup> on top of the grating, the thin film limit absorption can be increased to nearly 100%, and a perfect tunable graphene plasmonic absorber can be achieved. The calculations confirm that these resonances disappear when the graphene is absent, when the polarization is rotated parallel to the channels, or when the graphene is electrostatically gated to the charge neutral point. For comparison, in Figure 1d, we show the absorption spectrum for an array of electrically isolated graphene ribbons of identical width, carrier density, and mobility, which yields a far lower on-resonant absorption (blue curve), even when the fill-factor is increased to 50% (purple curve).

The nature of the fundamental metal–graphene plasmon resonance is illustrated in Figure 1e, which shows the charge density calculated at the resonant frequency. For comparison, we show in Figure 1f the charge density profile at plasmon resonance for an uncontacted graphene ribbon of the same dimension. In the contacted graphene, the metal regions act as capacitive reservoir for charge accumulation, and the graphene serves as an inductive channel, thus forming a resonant circuit that interacts strongly with the incident radiation. This is in striking contrast to the isolated ribbon case, where the coupling to incident radiation is weaker and does not depend sensitively on the grating period.<sup>4,5,17</sup> The extension of the spatial mode is accompanied by a significant reduction in the plasmon frequency (by a factor of  $\approx\sqrt{3}$  in comparison to that of an isolated graphene ribbon<sup>16</sup>). The factor  $\sqrt{3}$  is an approximate ratio that is consistent the postulate that a plasma wave incurs an approximate phase shift of approximately  $\pi/4$  upon reflection from an open boundary,<sup>20,21</sup> and  $3\pi/4$  upon reflection from a conductive boundary.

The optical properties of the metal–graphene plasmonic grating in the subwavelength limit ( $\Lambda < \lambda$ ) can be modeled by an equivalent two-port circuit at the junction of two semi-infinite transmission lines with impedances  $Z_0/\sqrt{\epsilon_1}$  and  $Z_0/\sqrt{\epsilon_2}$ , that represent the upper and lower regions respectively, as shown in Figure 2 ( $Z_0 = 377 \Omega$ , free space

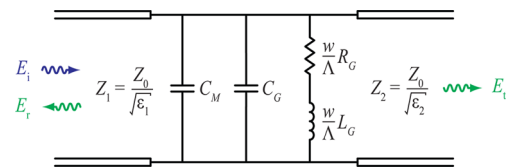


**Figure 2.** Two-port equivalent circuit used to model for the hybrid metal–graphene grating.  $R_G$  and  $L_G$  are the graphene ohmic resistance and kinetic inductance, respectively.  $C_G$  is the graphene ribbon array capacitance, and  $C_M$  is the capacitance of the metallic grid. The transmission ( $T = \sqrt{\epsilon_2/\epsilon_1} |E_t/E_i|^2$ ), reflection ( $R = |E_r/E_i|^2$ ), and graphene absorption ( $1-R-T$ ) can be approximately found from this circuit (Supporting Information S14,S15).  $Z_1 \equiv Z_0/\sqrt{\epsilon_1}$  and  $Z_2 \equiv Z_0/\sqrt{\epsilon_2}$  are wave impedances in the upper and lower semi-infinite regions with dielectric constants of  $\epsilon_1$  and  $\epsilon_2$ , respectively.

impedance). The graphene can be described by a Drude conductivity

$$\frac{1}{\sigma(\omega)} = \frac{(1 - i\omega/\Gamma)}{\sigma_0} = R_G - i\omega L_G \quad (1)$$

where  $\sigma_0 \equiv ne\mu$  represents the DC sheet conductivity of a graphene layer with carrier concentration  $n$  and mobility  $\mu$ , and  $\Gamma \equiv ev_F/\sqrt{\pi n}\mu\hbar$  is the scattering rate. From 1, the graphene may be modeled by its ohmic resistance,  $R_G = \sigma_0^{-1}$ , in series with its kinetic inductance,  $L_G = (\sigma_0\Gamma)^{-1}$ .<sup>22</sup>  $R_G$  and  $L_G$  must each be multiplied by a geometrical factor of  $w/\Lambda$  to account for the filling factor in this periodic structure. The conducting contacts act as a capacitive grid<sup>23,24</sup> that can be described by a capacitance  $C_M = 2\epsilon_0 \bar{\epsilon}\Lambda \ln(\csc(\pi w/2\Lambda)) / \pi$ , where  $\bar{\epsilon} = (\epsilon_1 + \epsilon_2) / 2$  is the average dielectric permittivity. The finite size graphene channels contribute to an additional parallel capacitance,<sup>25</sup> to give a total capacitance of  $C = C_M + C_G = 2\epsilon_0 \bar{\epsilon}\Lambda \ln(2\csc(\pi w/\Lambda)) / \pi$ . As shown in the Supporting Information (Figure S2), this circuit accurately models the transmission, reflection, and absorption for the lowest order plasmon mode. The plasmon resonance frequency of this circuit is found to be

$$\omega_0^2 = \frac{e^2 v_F \sqrt{\pi}}{2\hbar} \frac{\sqrt{n}}{w\epsilon_0 \bar{\epsilon} \ln[2\csc(\pi w/\Lambda)]} \quad (2)$$

As noted earlier, the resonant frequency scales in proportion to  $n^{1/4} w^{-1/2}$ , as for the case of uncontacted graphene ribbons considered in ref 4, indicating that  $\omega_0$  can be tuned through the application of a gate voltage or by adjusting the graphene channel width. The resonant frequency blue-shifts weakly with increasing the duty cycle  $w/\Lambda$ , but in all of the cases considered here the resonance frequency is lower than that of an uncontacted graphene ribbon of the same width. Equation 2 predicts that increasing the period  $\Lambda$  for a fixed width  $w$ , will result in a slight red shift of the plasmon frequency, which is in direct contrast to the case of uncontacted graphene ribbons, where the plasmon frequency is blue-shifted by increasing the period, as a result of reduced dipolar plasmon mode coupling in adjacent ribbons.<sup>17</sup>

The plasmon line width, computed from the equivalent circuit model, is found to be

$$\Delta\omega = \Gamma + \frac{\pi(Z_1^{-1} + Z_2^{-1})}{2\epsilon_0 \bar{\epsilon}\Lambda \ln[2\csc(\pi w/\Lambda)]} \quad (3)$$

The first term in eq 3 is the conventional Drude line width, which is constrained by the mobility and carrier density, whereas the second term describes the radiative line width of the plasmon, which does not depend on the graphene quality or material properties. This second term, which is negligible for uncontacted graphene ribbons, fundamentally limits the quality factor ( $Q = \omega_0/\Delta\omega$ ).

The equivalent circuit model can also be used to predict the condition under which maximum power is delivered to the graphene layer (Supporting Information S2). The maximum on-resonant graphene absorption is achieved when the material scattering rate  $\Gamma$  and radiative decay rates are equal, which also corresponds to the impedance matching between two dissimilar media.<sup>26,27</sup> For the parameters considered in Figure 1a, this matching condition occurs when  $\Lambda \approx 23w$ , which is consistent with Figure 1c. We note that this circuit model can be generalized by including an inductor<sup>22,26,27</sup> in series with  $C_M$  to

describe metal–graphene plasmonic devices coupled to antennas. In the circuit model, the metal was treated as a perfect conductor. This is a very good approximation when metal is gold with Drude conductivity ( $\Gamma = 3.33 \times 10^{13}$  rad/s,  $\omega_p = 1.36 \times 10^{16}$  rad/s). It is possible to account for the ohmic loss in the metal by adding a resistor in series with  $C_M$  in the equivalent circuit model.<sup>24</sup> However, for the typical dimensions, frequencies, and conductivities considered here, the series resistance is calculated to be much smaller than the reactance of the capacitive grid. We do not expect that this equivalent circuit model can be applied at infrared and optical frequencies, where the metallic structure has its own plasmonic behavior that cannot be ignored.<sup>28,29</sup>

Figure 3 shows a scanning-electron micrograph image of a device with  $w = 350$  nm and  $\Lambda = 7 \mu\text{m}$  that was used to study

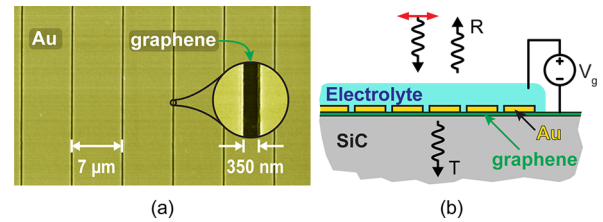


**Figure 3.** (a) The false-colored SEM image of the gold-graphene grating (top view).  $w = 350$  nm,  $\Lambda = 7 \mu\text{m}$ . (b) Diagram of the device with electrolyte top gate, and the reflection/transmission measurement scheme. The incident beam is polarized perpendicular to the gold strips.

the hybrid metal–graphene plasmons. Figure 4a shows the measured transmission as a function of frequency for different carrier density levels tuned by application of the gate voltage  $V_g$ . A resonant peak is observed in the transmission, which grows in strength and shifts to higher frequency with increasing carrier density. In reflection, the plasmon resonance exhibits a minimum that also becomes stronger and blue-shifts as the carrier density is increased (Figure 4b). In this figure, we present the reflection normalized to the lowest carrier density data to exhibit the plasmon resonance dip more clearly. The measured absorption ( $A = 1 - R - T$ ) is presented in Figure 4c, showing how the frequency and strength of THz resonant absorption can be controlled by tuning the carrier density with a gate voltage. The carrier density was extracted from the plasmon frequency at each gate voltage and by comparing the experimental spectra to finite element calculations.

Finite element calculations of the same measured quantities presented in Figure 4a and b are shown in Figure 4d and e, respectively, showing agreement with the experimental observations.

As with isolated graphene ribbons, the resonant frequency can also be changed by tailoring the width of the graphene channel, as predicted in 3, and confirmed experimentally in the Supporting Information. These results demonstrate how the hybrid metal–graphene resonances can be designed and tuned to produce strongly enhanced absorption at a chosen resonant frequency. These hybrid plasmon modes could also be incorporated in graphene-integrated metamaterials,<sup>22,30,31</sup> where the metal–graphene plasmon enhances the metamaterial resonance.

Finally, we note that these metal–graphene plasmonic structures can exhibit near 100% resonant transmission in a high mobility graphene sample, a feature that could be very

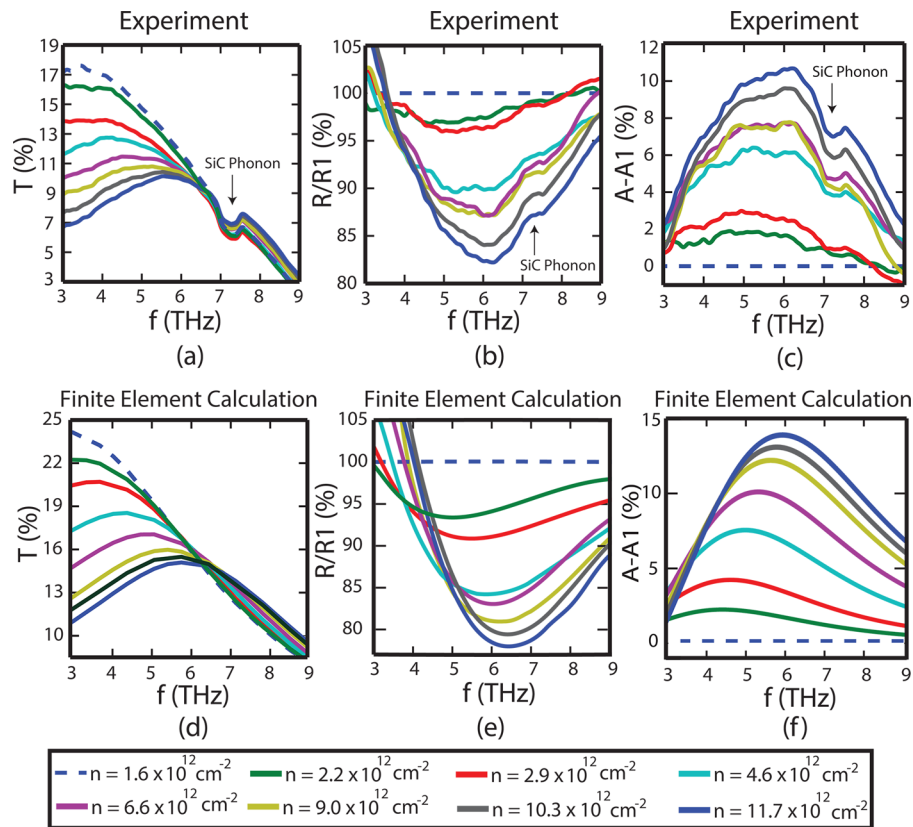


**Figure 4.** (a) Measured transmission spectrum ( $T$ ) for different carrier densities tuned by adjusting the gate voltage  $V_g$ . (b) Measured reflection ( $R$ ) off the device normalized relative to that measured with  $n = 1.6 \times 10^{12} \text{ cm}^{-2}$ , the lowest carrier density considered. (c) Measured absorption ( $A = 1 - R - T$ ) of the device, relative to that for the lowest carrier density ( $A_1$ ), demonstrating the gate-tunable absorption of the device. (d), (e), and (f) Finite element simulations of the transmission, reflection, and absorption respectively. The simulation parameters were set to match the experimental conditions, i.e.,  $w = 350 \text{ nm}$ ,  $\Lambda = 7 \text{ }\mu\text{m}$ ,  $\mu = 1010 \text{ cm}^2 \text{ V}^{-1} \text{ s}^{-1}$ .

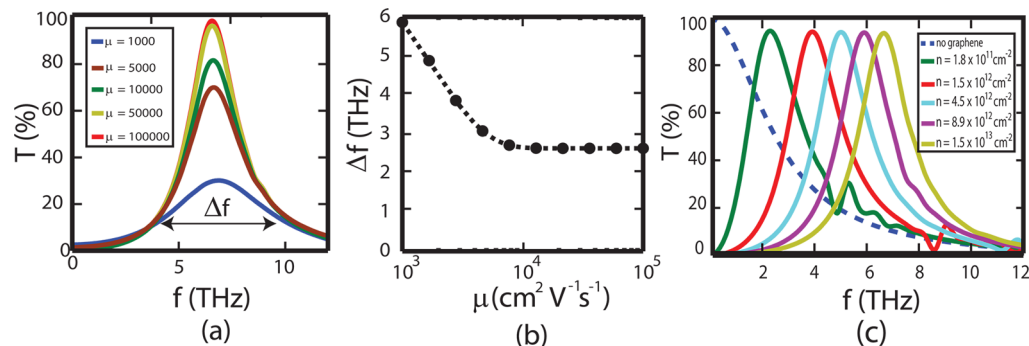


**Figure 5.** (a) Calculated transmission through the metal–graphene grating for different graphene mobility ( $\mu$ ) and  $n = 1.5 \times 10^{13} \text{ cm}^{-2}$ . (b) The plasmon resonance width as a function of graphene mobility. (c) Transmission through the meta-graphene grating for different carrier density levels.  $w = 350 \text{ nm}$ ,  $\Lambda = 7 \text{ }\mu\text{m}$ ,  $\mu = 50,000 \text{ cm}^2 \text{ V}^{-1} \text{ s}^{-1}$  at  $n = 1.5 \times 10^{13} \text{ cm}^{-2}$ . In all these results, the surrounding material was assumed to be uniform with  $\epsilon = 5$ .

useful in THz transmission filters or modulators. Figure 5a shows the calculated power transmission spectrum  $T(f)$  for the case of  $w/\Lambda = 1/20$ , and for graphene mobilities ranging from 1000 to 100 000  $\text{cm}^2 \text{ V}^{-1} \text{ s}^{-1}$  ( $n = 1.5 \times 10^{13} \text{ cm}^{-2}$ ). When the graphene mobility is increased, the graphene absorption decreases, but is replaced by a resonant peak in the transmission that approaches 100% transmission in the limit of high mobility. Again, we note that this resonance shifts to zero frequency<sup>23</sup> when the graphene is absent or charge-neutral, proving that the inductive graphene channel is essential to support the plasmonic resonance. As shown in Figure 5b, the

spectral width of this resonance decreases inversely with the mobility, but reaches a plateau in the limit of high mobility. Above this point, the plasmon line width is dominated by radiation damping and cannot be further reduced by improving the material quality, as predicted by eq 3. In contrast to isolated graphene ribbons, the plasmons in metal-contacted graphene are naturally radiative, a feature that can have important consequences in tunable graphene emitters or sensors. Figure 5c demonstrates the tunability of the near 100% resonant transmission through changing the graphene carrier density. The calculated transmission spectra also illustrate the existence

of higher order plasmon modes that are not described by the simple equivalent circuit model of Figure 2. The Supporting Information briefly considers these higher order modes and how they can be optimized.

**Methods. Sample and Device Preparation.** A single layer of graphene was formed on 8 mm × 8 mm semi-insulating (resistivity >10<sup>10</sup> Ω·cm) (0001)6H-SiC chips by the Si sublimation process in an Ar ambient. The substrates, misoriented from the basal plane by approximately 0.1°, were etched in H<sub>2</sub> prior to graphene synthesis.<sup>32</sup> Gold strips were fabricated on top of graphene using electron-beam lithography followed by Cr/Au (thickness: 5 nm/75 nm) thermal evaporation (Cr as the adhesion layer), and a lift-off process. The Au strips are 1.5 mm long and the whole grating is 1.5 mm wide creating a grating that has a 2.25 mm<sup>2</sup> area. To electrically isolate the grating from other parts of the graphene/SiC chip, a narrow ribbon (7 μm) was defined by electron-beam lithography using PMMA resist as a mask and oxygen plasma to remove the unmasked areas. Finally, electrolyte (poly(ethylene oxide)/LiClO<sub>4</sub>) was drop-cast on the sample as the top gate. The gate voltage was applied between the grating device and the other electrically isolated part of the SiC graphene substrate.

**FTIR Measurement.** Far infrared simultaneous transmission/reflection measurements are performed in a Bomem DA-8 FTIR system with mercury lamp as a source and two 4 K silicon composite bolometers as detectors. A polarizer is placed in the beam path and only passes polarization perpendicular to metal strips. The 1.5 × 1.5 mm<sup>2</sup> metal-graphene grating device is mounted on a copper plate with a 1.5 mm diameter aperture. The incident THz beam illuminated the back of the device making an angle about 10° from the normal. One bolometer is located on the transmitted beam path and one at the reflection side. A separate measurement on the sample without electrolyte was carried out to find and remove the electrolyte effect on the measured data.

**Numerical Simulations.** Frequency-domain finite element calculations were performed on a unit cell of the metal-graphene grating on top of the SiC substrate (refractive index = 3) with periodic boundary condition. The gold was modeled as a 75 nm thick Drude metal with  $\Gamma = 3.33 \times 10^{13}$  rad/s,  $\omega_p = 1.36 \times 10^{16}$  rad/s. The electrolyte on top of grating was modeled as a dielectric (refractive index = 1.7). Currents, fields, and charge density in graphene and metal were calculated. Transmission and reflection of an incident plane-wave, polarized perpendicular to the metal strips, were also calculated. In the carrier-density-dependent calculations, a constant scattering rate was assumed for graphene. Mobility was taken to be 1010 cm<sup>2</sup> V<sup>-1</sup> s<sup>-1</sup> at  $n = 5 \times 10^{12}$  cm<sup>-2</sup>, based on van der Pauw Hall measurements taken on the full graphene on SiC sample prior to processing. In the finite element calculations Fermi-level pinning at graphene-metal junction<sup>33</sup> was ignored. A constant Fermi level across the graphene channel and zero graphene-metal contact resistance were assumed. The close agreement between experimental results and theory suggest that the Fermi-level pinning and nonzero contact resistance effects are negligible in the devices we studied. However, we expect that they should have a noticeable effect for narrow graphene channels (<100 nm).<sup>33</sup>

## ■ ASSOCIATED CONTENT

### Supporting Information

The Supporting Information is available free of charge on the ACS Publications website at DOI: 10.1021/acs.nanolett.5b03191.

The Supporting Information contains four subsections: (1) Detailed description of the integral equation method for finding plasmon modes in a metal-graphene grating. (2) Equivalent circuit model and the related analysis. (3) Experimental data on metal-graphene gratings with different graphene channel widths. (4) Discussion on higher order hybrid plasmon modes in the metal-graphene structure. (PDF)

## ■ AUTHOR INFORMATION

### Corresponding Authors

- \* E-mail: mmjadidi@umd.edu.
- \* E-mail: kurt.gaskill@nrl.navy.mil.
- \* E-mail: michael.fuhrer@monash.edu.
- \* E-mail: hdrew@umd.edu.
- \* E-mail: tem@umd.edu.

### Notes

The authors declare no competing financial interest.

## ■ ACKNOWLEDGMENTS

This work was sponsored by the U.S. ONR (N000141310865) and the U.S. NSF (ECCS 1309750). Work at NRL was supported by the Office of Naval Research.

## ■ REFERENCES

- (1) Fei, Z.; Rodin, A. S.; Andreev, G. O.; Bao, W.; McLeod, A. S.; Wagner, M.; Zhang, L. M.; Zhao, Z.; Thieme, M.; Dominguez, G.; Fogler, M. M.; Neto, A. H. C.; Lau, C. N.; Keilmann, F.; Basov, D. N. *Nature* **2012**, *487*, 82–85.
- (2) Chen, J.; Badioli, M.; Alonso-González, P.; Thongrattanasiri, S.; Huth, F.; Osmond, J.; Spasenović, M.; Centeno, A.; Pesquera, A.; Godignon, P.; Elorza, A. Z.; Camara, N.; de Abajo, F. J. G.; Hillenbrand, R.; Koppens, F. H. L. *Nature* **2012**, *487*, 77–81.
- (3) Vakil, A.; Engheta, N. *Science* **2011**, *332*, 1291–1294.
- (4) Ju, L.; Geng, B.; Horng, J.; Girit, C.; Martin, M.; Hao, Z.; Bechtel, H. A.; Liang, X.; Zettl, A.; Shen, Y. R.; Wang, F. *Nat. Nanotechnol.* **2011**, *6*, 630–634.
- (5) Yan, H.; Li, X.; Chandra, B.; Tulevski, G.; Wu, Y.; Freitag, M.; Zhu, W.; Avouris, P.; Xia, F. *Nat. Nanotechnol.* **2012**, *7*, 330–334.
- (6) Rodrigo, D.; Limaj, O.; Janner, D.; Etezadi, D.; de Abajo, F. J. G.; Pruneri, V.; Altug, H. *Science* **2015**, *349*, 165–168.
- (7) Cai, X.; Sushkov, A. B.; Jadidi, M. M.; Nyakiti, L. O.; Myers-Ward, R. L.; Gaskill, D. K.; Murphy, T. E.; Fuhrer, M. S.; Drew, H. D. *Nano Lett.* **2015**, *15*, 4295–4302.
- (8) Brar, V. W.; Sherrott, M. C.; Jang, M. S.; Kim, S.; Kim, L.; Choi, M.; Sweatlock, L. A.; Atwater, H. A. *Nat. Commun.* **2015**, *6*, 7032.
- (9) Hartmann, R. R.; Kono, J.; Portnoi, M. E. *Nanotechnology* **2014**, *25*, 322001.
- (10) Vicarelli, L.; Vitiello, M. S.; Coquillat, D.; Lombardo, A.; Ferrari, A. C.; Knap, W.; Polini, M.; Pellegrini, V.; Tredicucci, A. *Nat. Mater.* **2012**, *11*, 865–871.
- (11) Cai, X.; Sushkov, A. B.; Suess, R. J.; Jadidi, M. M.; Jenkins, G. S.; Nyakiti, L. O.; Myers-Ward, R. L.; Li, S.; Yan, J.; Gaskill, D. K.; Murphy, T. E.; Drew, H. D.; Fuhrer, M. S. *Nat. Nanotechnol.* **2014**, *9*, 814–819.
- (12) Sensale-Rodriguez, B.; Yan, R.; Kelly, M. M.; Fang, T.; Tahy, K.; Hwang, W. S.; Jena, D.; Liu, L.; Xing, H. G. *Nat. Commun.* **2012**, *3*, 780.

- (13) Lee, S. H.; Choi, M.; Kim, T.-T.; Lee, S.; Liu, M.; Yin, X.; Choi, H. K.; Lee, S. S.; Choi, C.-G.; Choi, S.-Y.; Zhang, X.; Min, B. *Nat. Mater.* **2012**, *11*, 936–941.
- (14) Shi, S.-F.; Zeng, B.; Han, H.-L.; Hong, X.; Tsai, H.-Z.; Jung, H. S.; Zettl, A.; Crommie, M. F.; Wang, F. *Nano Lett.* **2015**, *15*, 372–377.
- (15) Tong, J.; Muthee, M.; Chen, S.-Y.; Yngvesson, S. K.; Yan, J. *Nano Lett.* **2015**, *15*, 5295–5301.
- (16) Mikhailov, S. A.; Savostianova, N. A. *Phys. Rev. B: Condens. Matter Mater. Phys.* **2006**, *74*, 045325.
- (17) Nene, P.; Strait, J. H.; Chan, W.-M.; Manolatu, C.; Tiwari, S.; McEuen, P. L.; Rana, F. *Appl. Phys. Lett.* **2014**, *105*, 143108.
- (18) Hilsom, C. J. *Opt. Soc. Am.* **1954**, *44*, 188–191.
- (19) Jang, M. S.; Brar, V. W.; Sherrott, M. C.; Lopez, J. J.; Kim, L.; Kim, S.; Choi, M.; Atwater, H. A. *Phys. Rev. B: Condens. Matter Mater. Phys.* **2014**, *90*, 165409.
- (20) Nikitin, A. Y.; Low, T.; Martin-Moreno, L. *Phys. Rev. B: Condens. Matter Mater. Phys.* **2014**, *90*, 041407.
- (21) Velizhanin, K. A. *Phys. Rev. B: Condens. Matter Mater. Phys.* **2015**, *91*, 125429.
- (22) Yao, Y.; Kats, M. A.; Genevet, P.; Yu, N.; Song, Y.; Kong, J.; Capasso, F. *Nano Lett.* **2013**, *13*, 1257–1264.
- (23) Ulrich, R. *Infrared Phys.* **1967**, *7*, 37–55.
- (24) Whitbourn, L. B.; Compton, R. C. *Appl. Opt.* **1985**, *24*, 217–220.
- (25) Chen, P.-Y.; Alù, A. *IEEE Trans. Terahertz Sci. Technol.* **2013**, *3*, 748–756.
- (26) Balanis, C. A. *Antenna theory analysis and design*, 3rd ed.; John Wiley: Hoboken, NJ, 2012.
- (27) Alù, A.; Engheta, N. *Phys. Rev. Lett.* **2008**, *101*, 043901.
- (28) Alù, A.; Engheta, N. *IEEE Trans. Antennas Propag.* **2013**, *61*, 1508–1517.
- (29) Carter, F. W.; Santavicca, D. F.; Prober, D. E. *Opt. Express* **2014**, *22*, 22062–22071.
- (30) Mousavi, S. H.; Kholmanov, I.; Alici, K. B.; Purtseladze, D.; Arju, N.; Tatar, K.; Fozdar, D. Y.; Suk, J. W.; Hao, Y.; Khanikaev, A. B.; Ruoff, R. S.; Shvets, G. *Nano Lett.* **2013**, *13*, 1111–1117.
- (31) Ferreira, A.; Peres, N. M. R. *Phys. Rev. B: Condens. Matter Mater. Phys.* **2012**, *86*, 205401.
- (32) Nyakiti, L.; Wheeler, V.; Garces, N.; Myers-Ward, R., Jr.; Eddy, C. R.; Gaskill, D. *MRS Bull.* **2012**, *37*, 1149–1157.
- (33) Khomyakov, P. A.; Starikov, A. A.; Brocks, G.; Kelly, P. J. *Phys. Rev. B: Condens. Matter Mater. Phys.* **2010**, *82*, 115437.